

## TEM study of fracturing in spherical and plate-like LiFePO<sub>4</sub> Particles

H. Gabrisch<sup>a</sup>, J. Wilcox<sup>b</sup>, and M. M. Doeff<sup>b</sup>

<sup>a</sup> Department of Chemistry, Advanced Materials Research Institute, University of

New Orleans, New Orleans, LA 70148

<sup>b</sup> Materials Sciences Division

Lawrence Berkeley National Laboratory, University of California Berkeley, CA

94720

### *Abstract*

An investigation of fracturing in LiFePO<sub>4</sub> particles as a function of the particle morphology and history is presented. Two types of samples, one subjected to electrochemical cycling and another to chemical delithiation are compared. We observe the formation of micro fractures parallel to low indexed lattice planes in both samples. The fracture surfaces are predominantly parallel to (100) planes in the chemically delithiated powder and (100) and (010) planes in the electrochemically cycled powder. A consideration of the threshold stresses for dislocation glide shows that particle geometry plays an important role in the observed behavior.

Key words : LiFePO<sub>4</sub>, fractures, TEM

## Introduction

LiFePO<sub>4</sub> was first introduced in 1997 by Padhi et al. as a cathode material for rechargeable Li-ion batteries.<sup>1</sup> The natural abundance of LiFePO<sub>4</sub>, its non-toxicity, and a high theoretical capacity of 170 mAh/g make it a promising candidate for battery applications in electric and hybrid vehicles.<sup>1, 2</sup> In its native state, LiFePO<sub>4</sub> has low electronic conductivity, which limits the rate at which it can be discharged. Strategies to enhance the electrochemical performance include reduction of the particle size<sup>3</sup>, carbon coating<sup>4-6</sup>, doping<sup>7, 8</sup> and addition of small metallic particles.<sup>9</sup> Batteries with carbon-coated nanoparticulate LiFePO<sub>4</sub> have very high rate capabilities and are now being considered for use in hybrid electric vehicles (HEVs). Further commercialization (e.g., for higher energy density applications such as plug-in hybrid electric vehicles (PHEVs)) require that care be taken with these approaches, however, as they may result in a reduction of the practical energy density.<sup>10</sup> We have shown that electronic conductivity and rate performance can be enhanced considerably without a substantial increase in carbon content by choosing synthetic additives that increase the graphitic nature of the coatings.<sup>11</sup> TEM studies on these materials show that a carbon layer thickness of about 10 nm is sufficient to improve the electrochemical behavior.<sup>12</sup> For PHEV and other higher energy density applications, the coatings on the LiFePO<sub>4</sub> particles must remain reasonably intact over many moderately deep charge-discharge cycles. The possibility of particle fracture due to the stresses of repeated delithiation and relithiation also bears relevance to cycle life.

LiFePO<sub>4</sub> (triphylite) and the delithiated phase FePO<sub>4</sub> (heterosite) belong to the group of phospho-olivines having an orthorhombic unit cell (SG 62, Pnma symmetry). The crystal lattice is formed by a distorted hexagonal close packed stacking of oxygen ions

with Fe and Li ions on octahedral interstitial sites and phosphorus in tetrahedral coordination. As a result of the three dimensional arrangement of  $\text{PO}_4$  tetrahedra and  $\text{FeO}_6$  octahedra, tunnels parallel to [010] and [100] directions provide pathways for lithium diffusion. Experimental transport measurements on  $\text{LiFePO}_4$  single crystals indicate that electron and ion transport is faster in [010] and [001] directions than along [100], while theoretical calculations predict that the migration of Li ions takes place primarily in the [010] direction with the Li pathway following a curved trajectory.<sup>13-15</sup> The de-intercalation of Li from the crystal lattice during charge of the battery proceeds via a two-phase reaction, in which the fully lithiated triphylite is transformed into heterosite ( $\text{FePO}_4$ ). The accompanying changes in the unit cell dimensions give rise to considerably large misfit stresses between the two phases ( $\text{LiFePO}_4$  :  $a=10.33\text{\AA}$ ,  $b=6.01\text{\AA}$ ,  $c=4.69\text{\AA}$  ;  $\text{FePO}_4$  :  $a=9.81\text{\AA}$ ,  $b=5.79\text{\AA}$ ,  $c=4.78\text{\AA}$ ).<sup>16</sup> This can lead to fracturing when threshold stresses in either phase are exceeded. The relationship between micro fractures and the orientation of the triphylite/heterosite interface is, at present, unknown. However, there has been some speculation that micro fractures contribute to failure of cathodes based on  $\text{LiFePO}_4$ .<sup>17,18</sup>

In the original paper,<sup>1</sup> Padhi introduced a simplified core shell model for the distribution of the two phases in  $\text{Li}_x\text{FePO}_4$ . The highly anisotropic unit cell of  $\text{LiFePO}_4$  and the resulting directionality of Li diffusion, however, argue against this interpretation. Recently Chen et al.<sup>17</sup> investigated  $\text{LiFePO}_4$  before and after chemical delithiation by Transmission Electron Microscopy (TEM). At the composition of  $\text{Li}_{0.5}\text{FePO}_4$ , the authors observed stripes of alternating contrast parallel to (100) planes that were sometimes separated by fractures. The Fourier transform of a high-resolution image taken from a thin region of a  $\text{Li}_{0.5}\text{FePO}_4$  particle indicates that stripes of  $\text{LiFePO}_4$  and  $\text{FePO}_4$  extend parallel to the (100) planes. Similarly in a study by high-resolution electron energy loss it

was concluded that zones of alternating  $\text{FePO}_4$  and  $\text{LiFePO}_4$  composition are present in  $\text{Li}_x\text{FePO}_4$  particles.<sup>19</sup> While the results of both studies are not in perfect agreement, they revive the debate about the location of the  $\text{LiFePO}_4/\text{FePO}_4$  interface.

In the present study, the microstructure of  $\text{LiFePO}_4$  subjected to electrochemical cycling is compared to that of  $\text{LiFePO}_4$  obtained by chemical delithiation. We find that micro cracks form in both specimens, differing only in the orientation of the fracture surfaces. Assuming that the fracture mechanism is dislocation based, the observations can be reconciled considering the threshold stresses that need to be overcome for dislocation glide.

### Experimental

$\text{LiFePO}_4$  for use in electrodes was synthesized by a sol gel method from iron nitrate, lithium acetate, phosphoric acid and glycolic acid precursors as detailed in reference<sup>11</sup>. Laminated electrodes containing 80 wt % active material, 8 wt % Kynar polyvinylidene fluoride, 6 wt % SFG-6 synthetic flake graphite, and 6 wt % compressed acetylene black were prepared with loadings of about 1 mAh/cm<sup>2</sup> of active material. 2032 size coin cells were assembled in a helium-filled glove box, using lithium metal as a counter electrode and 1 M  $\text{LiPF}_6$  in 1:2 ethylene carbonate/dimethyl carbonate (EC/DMC) as the electrolytic solution with Celgard 3401 as the separator. The cells were cycled galvanostatically between 2.0 and 3.9V at C/25 charge rate using an Arbin BT/HSP-2043 cycler. Most discharges for cell 1 were carried out at C/25 rate and at C/2 rate for cell 2. After approximately 100 cycles, the cells were stopped in the approximately fully discharged state and disassembled. The graphite/binder/powder mixture was scraped off the Al collectors and washed repeatedly in NMP to dissolve the binder followed by a wash in acetone.

LiFePO<sub>4</sub>, prepared by hydrothermal synthesis and chemically delithiated Li<sub>0.5</sub>FePO<sub>4</sub><sup>17</sup> were obtained courtesy of Dr. Thomas Richardson of Lawrence Berkeley National Laboratory. For TEM specimen preparation, the powders were dispersed in acetone or ethanol and the solutions were transferred onto a holey carbon grid. Care was given not to crush the specimens during preparation.

TEM investigations were performed using a JEOL 3010 operated at 200kV at the National Center for Electron Microscopy at Lawrence Berkeley National Laboratory and a JEOL 2010 at the University of New Orleans operated at 200kV. Tilting experiments for imaging in dark-field conditions were performed at the Technical University of Berlin/Germany using a Philips CM300 operated at 200kV. The accelerating voltage 300kV was used briefly to investigate the stability of Li<sub>x</sub>FePO<sub>4</sub> particles at higher accelerating voltages but proved unsuitable for delithiated compounds. Experimentally obtained electron diffraction patterns were compared to electron diffraction patterns simulated with the software packet Desktop Microscopist using unit cells published in literature<sup>2</sup>.

## Results

In Figure 1, the cycling data for cell 1 (discharged at C/25) and cell 2 (discharged at C/2) is shown. The specific discharge capacities initially increase with cycle number and then level off to values of 145 mAh/g and 125 mAh/g, respectively. The specific capacity of cell 2, cycled at the higher discharge rate, declines after about 60 cycles, while the performance of cell 1 remains stable.

Uncycled LiFePO<sub>4</sub> synthesized by the sol gel method has a compact particle shape with arbitrary surface orientations and an average particle size of 200 nm (estimated from the Scherrer equation). A characterization of the pristine material and its carbon coating

has been published in reference <sup>12</sup>. In particles retrieved from the cycled cells, the carbon surface layer is still intact regardless of surface orientation. An example is shown in Figure 2, which shows a particle from cell 1 in [011] orientation. In the diffraction patterns of the cycled particles, spot splitting at reflections further away from the incident beam was occasionally observed, indicating that a two-phase microstructure has formed (see arrow in Fig. 2b). (Some FePO<sub>4</sub> is present even in nominally fully discharged cells, due to coulombic inefficiencies and/or cycling losses.) The most prominent feature in particles from both cycled cells is the formation of large fractures parallel to low indexed lattice planes. The cracks start at the specimen surface and extend into the interior of the particle. Examples of particles with micro fractures taken from cell 1 and cell 2 are shown in Figures 3a and c, together with the corresponding diffraction patterns in Figures 3b and d. The fracture surfaces are oriented parallel to (010) and (100) planes in the electrochemically cycled LiFePO<sub>4</sub>.

For comparison, we also studied the hydrothermally prepared samples of LiFePO<sub>4</sub> before and after chemical delithiation to a nominal composition of Li<sub>0.5</sub>FePO<sub>4</sub>. The as-made particles have plate-like morphologies with [010] surface plane normal. The platelets are elongated in the [001] direction and have average dimensions (length x width x height) of 4μm x 2μm x 0.2μm. Due to the preferred orientation and small tilt angles used in the TEM, the plate-like particles are observed mostly in the [010] projection. Figure 4 shows an example of a fracture observed in the chemically delithiated specimen. The fracture surfaces shown here and observed in other particles of this sample are parallel to (100) planes in agreement with the original published data. <sup>17</sup> The number of fractures observed in the chemically delithiated material is considerably higher than in the electrochemically cycled powders, underlining the correlation between internal stresses and particle fracturing. The magnitude of misfit stresses in the system

$\text{LiFePO}_4/\text{FePO}_4$  is expected to be highest at a lithium content  $x=0.5$ , however high lithium extraction rates like those used in chemical delithiation add to the magnitude of internal stresses.<sup>20, 21</sup> Dark field images of a particle from a cycled cell and of a delithiated particle  $\text{Li}_{0.5}\text{FePO}_4$  are shown in Figure 5a and 5c, together with the corresponding diffraction patterns (Figures 5b and 5d). Under dark field imaging conditions, dislocations are visible as bright lines on a dark background. The comparison shows that the dislocation density is much higher in the chemically delithiated particle than in the cycled particle that has passed through the composition  $\text{Li}_{0.5}\text{FePO}_4$  about 200 times (but was removed from the cell and studied in the discharged state).

### Discussion

In order to understand the different orientations of fracture surfaces observed in the two different samples, the geometry of fractures formed by breaking of bonds between  $\text{FeO}_6$  and  $\text{PO}_4$  polyhedra should be considered. Assuming that dislocation glide is responsible for the formation of the observed cracks, we can then estimate the minimum force necessary to activate dislocation glide in different  $\{100\}$  planes.

Figure 6 shows a schematic drawing of the olivine structure in  $[001]$  projection where  $(100)$  and  $(010)$  planes are seen edge on. The bonds between  $(100)$  planes and between  $(010)$  planes are marked by dashed circles and by full circles, respectively. It can be seen that  $(100)$  planes are connected through shared corners between  $\text{FeO}_6$  octahedra and  $\text{PO}_4$  tetrahedra, while  $(010)$  planes are linked by edge sharing bonds between  $\text{FeO}_6$  octahedra. According to the Third Pauli's Rule on bond strength between coordination polyhedra, corner-sharing bonds are more stable than edge sharing and face sharing bonds.<sup>22</sup> Therefore, in a first approximation, a higher driving force is required to break the bonds

between (100) planes compared to breaking the bonds between (010) planes, favoring (010) fracture surfaces.

Switching viewing directions, we consider the role of internal stresses in particle fracturing by comparing the elastic stress fields of dislocations in  $\{100\}$  planes of spherical and plate like particles. Dislocations are one dimensional lattice defects that can be described by a displacement of atoms from their original lattice sites. They are characterized by a Burgers vector,  $\vec{b}$ , representing the direction and distance of atom displacement and a line direction,  $\vec{s}$ , along which actual atom positions deviate from their assigned lattice sites.<sup>23</sup> The angle  $\varphi$  between the Burgers vector,  $\vec{b}$  and the dislocation line direction,  $\vec{s}$ , determines the character of a dislocation, with limiting cases  $\varphi = 0^\circ$  for a screw dislocation, and  $\varphi = 90^\circ$  for an edge dislocation. Edge dislocations can be visualized as an extra half-plane inserted into the crystal perpendicular to the Burgers vector, ending at the dislocation line. It follows that the edge component of a dislocation located in a 2-phase interface relaxes misfit stresses between the two phases rendering the interface semi-coherent. Under application of a shear force a dislocation glides in the plane spanned by the Burgers vector and the dislocation line direction, called the glide plane of the dislocation\*. The combination of a glide plane, symbolized by its plane normal  $\vec{n}$  and a dislocation's Burgers vector, form a glide system. Geometrical considerations show that dislocations moving in different glide planes result in the formation of differently oriented fracture surfaces. In Figure 7, the dislocation lines and Burgers vectors for misfit dislocations with  $\langle 100 \rangle$  type Burgers vectors in  $\{100\}$  type planes are shown for an orthorhombic unit cell. It can be seen that in the (100) plane, misfit dislocations have either [010] or [001] Burgers vectors and [001] or [010] line

---

\* The Burgers vector of screw dislocations is parallel to the dislocation line; as a result no distinct glide plane exists.



directions, respectively. In the (010) plane, misfit dislocations have [100] and [001] Burgers vectors and [001] and [100] directions, respectively.

The elastic strain caused by the presence of a dislocation in a crystalline material gives rise to stresses that are proportional to the Burgers vector  $\vec{b}$  and the material's bulk modulus  $G$ . For isotropic materials, it follows that the elastic stress is lowest for dislocations with the shortest Burger vectors. However in  $\text{LiFePO}_4$ , which has strong anisotropic properties, the directionality of the bulk modulus and the length of the Burgers vectors need to be taken into account for comparisons between dislocations. We estimate qualitative differences between the elastic stress fields of dislocations with  $\langle 100 \rangle$  type Burgers vectors in triphylite using elastic moduli calculated from first principles by Maxisch and Ceder.<sup>24</sup> In Table 1, the products  $G\vec{b}$  for the dislocations considered here are listed together with the values used for the elastic moduli in the direction of the Burgers vectors (note that these considerations do not include the dislocations' character). Comparison shows that a dislocation with a Burgers vector  $\vec{b}=[001]$  that is glissile in (100) and (010) planes induces the lowest elastic stress per unit length [N/m]. For the activation of the dislocation glide, a shear force that overcomes the elastic stress needs to act in the glide plane in the direction of the Burgers vector. The forces required for a given dislocation can be calculated from the dislocation line length and the elastic stress per unit length that depends on the Burgers vector. For a dislocation with Burgers vector  $\vec{b}=[001]$ , the line directions are [100] on the (010) plane and [010] on the (100) plane (see Figure 7). In the case of spherical particles like those that were electrochemically cycled for this study, the line length is independent of orientation so that dislocations with Burgers vector  $\vec{b}=[001]$  are equally likely to be activated in (100) and (010) planes, leading to fracturing between these planes. In comparison, the

dimensions of the chemically delithiated plate-like particles increase along the three  $\langle 100 \rangle$  orientations in the order  $L_{[010]}=0.2\mu\text{m} < L_{[100]}=2\mu\text{m} < L_{[001]}=4\mu\text{m}$ . As a result, a dislocation with Burgers vector  $\vec{b}=[001]$  requires a lower force for activation of glide on the (100) plane having a [010] line direction than on the (010) plane where it has a [100] line direction. The forces required to overcome the elastic stresses of misfit dislocations in spherical and plate like particles are summarized in Table 2. It can be seen that the lowest threshold exists for dislocations having [001] Burgers vectors, gliding on (100) and (010) planes in spherical particles and on (100) planes in the plate-like particles. This is in agreement with our experimental observations. A comparison of the calculated numbers shows that the forces required to overcome the dislocation's stress field in (100) planes are about 10 times smaller for the plate-like morphology than for spherical particles, underlining the effect of particle size.

### Conclusions

We observed fractures in  $\text{LiFePO}_4$  subjected to electrochemical cycling and to chemical delithiation. For the former, the particle geometry was spherical, and fracture surfaces of (100) and (010) orientations were observed. In contrast, the chemically treated samples had a plate-like morphology and only fractures with a (100) surface plane orientation were observed. The number of fractures and the dislocation density were higher after chemical delithiation than after electrochemical cycling, indicating the effect of composition and lithium extraction rate on the magnitude of the internal stresses. Estimates of dislocation stress fields in different particle geometries show that dislocations with Burgers vector [001] which are glissile in (100) and (010) planes are likely to be activated on both planes in spherical particles but will only be activated on (100) planes in the plate-like particles.

### **Acknowledgments**

The authors thank Dr. Guoying Chen for preparation of the delithiated  $\text{Li}_{0.5}\text{FePO}_4$  powders. This work was supported by DARPA under contract number HR0011-04-1-0029, the Office of Science, Office of Basic Energy Sciences, of the U.S. Department of Energy under Contract No. DE-AC02-05CH11231, the Office of Basic Energy Sciences, of the U.S. Department of Energy under Contract No. DE-AC02-05CH11231 and the Office of FreedomCAR and Vehicle Technologies of the U.S. Department of Energy under contract no. DE-AC02-05CH11231.

## References

1. A. K. Padhi, K. S. Nanjundaswami, and J. B. Goodenough, *J. Electrochem. Soc.*, **144**, 1188 (1997).
2. O. Haas, A. Deb, E. J. Cairns, and A. Wokaun, *J. Electrochem. Soc.*, **152**, A191 (2005).
3. A. Yamada, S. C. Chung, and K. Hinokuma, *J. Electrochem. Soc.*, **148**, A224 (2001).
4. N. Ravet, J. B. Goodenough, S. Besner, M. Simoneau, P. Hovington, and M. Armand, *The Electrochemical Society and the Electrochemical Society of Japan Meeting*, Honolulu (1999).
5. Z. Chen, Z. Lu, and J. R. Dahn, *J. Electrochem. Soc.*, **149**, A1604 (2002).
6. K. Zaghib, J. Shim, A. Guerfi, P. Charest, and K. Striebel, *Electrochem. Solid-State Lett.*, **8**, A207 (2005).
7. S.-Y. Chung, J. T. Bloking, and Y.-M. Chiang, *Nat. Mater.*, **1**, 123 (2002).
8. S. P. Herle, B. Ellis, N. Coombs, and L. F. Nazar, *Nat. Mater.*, **3**, 147 (2004).
9. F. Croce, A. D. Epifanio, J. Hassoun, A. Deptula, T. Olczac, and B. Scrosati, *Electrochem. Solid-State Lett.*, **5**, A47 (2002).
10. Z. Chen and J. R. Dahn, *J. Electrochem. Soc.*, **140**, A1184 (2002).
11. J. D. Wilcox, M. M. Doeff, M. Marcinek, and R. Kostecki, *J. Electrochem. Soc.*, **154**, A389 (2007).
12. H. Gabrisch, J. D. Wilcox, and M. M. Doeff, *Electrochem. Solid-State Lett.*, **9**, A360 (2006).
13. D. Morgan, A. Van der Ven, and G. Ceder, *Electrochem. Solid-State Lett.*, **7**, A30 (2004).

14. S. M. Islam, D. J. Driscoll, C. A. J. Fisher, and P. R. Slater, *Chem. Mater.*, **17**, 5085 (2005).
15. R. Amin, P. Balaya, and J. Maier, *Electrochem. Solid-State Lett.*, **10**, A13 (2007).
16. A. S. Andersson, B. Kalska, L. Haeggstroem, and J. O. Thomas, *Solid State Ionics*, **130**, 41 (2000).
17. G. Chen, X. Song, and T. J. Richardson, *Electrochem. Solid-State Lett.*, **9**, A295 (2006).
18. D. Wang, X. Wu, Z. Wang, and L. Chen, *J. Power Sources*, **140**, 125 (2005).
19. L. Laffont, C. Delacourt, P. Gibot, M. Y. Wu, P. Kooyman, C. Masquelier, and J. M. Tarascon, *Chem. Mater.*, **18**, 5520 (2006).
20. H. Gabrisch, Q. Xing, and T. Yi, *212<sup>th</sup> ECS Meeting*, edited by M. Smart, K. Abraham and R. Bugga (The Electrochemical Society of America, Washington, D.C., 2007), Vol. B11, #661.
21. X. Zhang, W. Shyy, and A. M. Sastry, *J. Electrochem. Soc.* **154**, A910 (2007).
22. C. Giacovazzo, H. L. Monaco, G. Artioli, D. Viterbo, G. Ferraris, G. Gilli, G. Zanotti, and M. Catti, *Fundamentals of Crystallography* (Oxford University Press, Oxford, 2002).
23. J. P. Hirth and J. Lothe, *Theory of dislocations* (John Wiley and Sons, 1982).
24. T. Maxisch and G. Ceder, *Phy. Rev. B*, **73**, 174112 (2006).

**Table 1**

<i>Direction of Burgers vector <math>\vec{b}</math></i>	<i>Magnitude of <math>\vec{b}</math> [10<sup>-10</sup> m]</i>	<i>Directional Bulk Moduli [10<sup>9</sup> Pa]<sup>23</sup></i>	<i>G<math>\vec{b}</math> [N/m]</i>
[100]	10.33	207	214
[010]	6.01	459	276
[001]	4.70	279	131

Table 1 : Comparison of elastic stresses for dislocations having <100> type Burgers vectors in LiFePO<sub>4</sub>.

**Table 2**

$\bar{n}$	$\bar{b}$	$\bar{s}$	$L_{\bar{s}}$ (sphere) [10 <sup>-6</sup> m]	$L_{\bar{s}}$ (plate) [10 <sup>-6</sup> m]	$F_{\bar{b}}$ (sphere) [10 <sup>-5</sup> N]	$F_{\bar{b}}$ (plate) [10 <sup>-4</sup> N]
(100)	[010]	[001]	0.2	4.0	5.52	11.03
	[001]	[010]	0.2	0.2	2.62	0.26
(010)	[100]	[001]	0.2	4.0	4.28	8.56
	[001]	[100]	0.2	2.0	2.62	2.62
(001)	[100]	[010]	0.2	0.2	4.28	0.43
	[010]	[100]	0.2	2.0	5.52	5.52

**Table 2.** Forces  $F_{\bar{b}}$  required for overcoming elastic stresses of misfit dislocations in {100} planes in LiFePO<sub>4</sub>. For each Burgers vector  $\bar{b}$  a line direction  $\bar{s}$  is given followed by the length of a dislocation parallel to  $\bar{s}$  in spherical particles ( $L_{\bar{s}}$  sphere) and in plate like particles ( $L_{\bar{s}}$  plate). The corresponding forces required in plate like particles and in spheres are listed in the last two columns. The numerical values for the estimated forces reflect qualitative differences between different glide systems in the specified geometries, not absolute numbers.

## Figure Captions

Figure 1. Capacity as a function of cycle number for cells 1 and 2. Both were charged at C/25 rate. Most discharges were carried out at C/25 rate for cell 1 and C/2 rate for cell 2.

Figure 2. a) Image of a particle retrieved from cell 1, showing (100) lattice planes and an intact carbon surface layer. b) Corresponding diffraction pattern in the [011] zone axis orientation showing spot splitting at some outer reflections (see arrow).

Figure 3. Image and diffraction patterns taken from  $\text{LiFePO}_4$  particles retrieved from cell 1 (Fig. 3a, b) and cell 2 (Fig. 3c, d). The fracture surfaces are oriented parallel to (100) and (010) planes.

Figure 4. Image and diffraction pattern taken from  $\text{Li}_{0.5}\text{FePO}_4$  synthesized from hydrothermally produced  $\text{LiFePO}_4$ . The fracture surface is oriented parallel to (100) planes. In the diffraction pattern, spot splitting typical for the two-phase microstructure is observed.

Figure 5, Dark field images and corresponding diffraction patterns of particles retrieved from cycled cell 2 (a and b) and a chemically delithiated  $\text{Li}_{0.5}\text{FePO}_4$  particle (Fig. 5c and d). The comparison illustrates the difference in dislocation density.

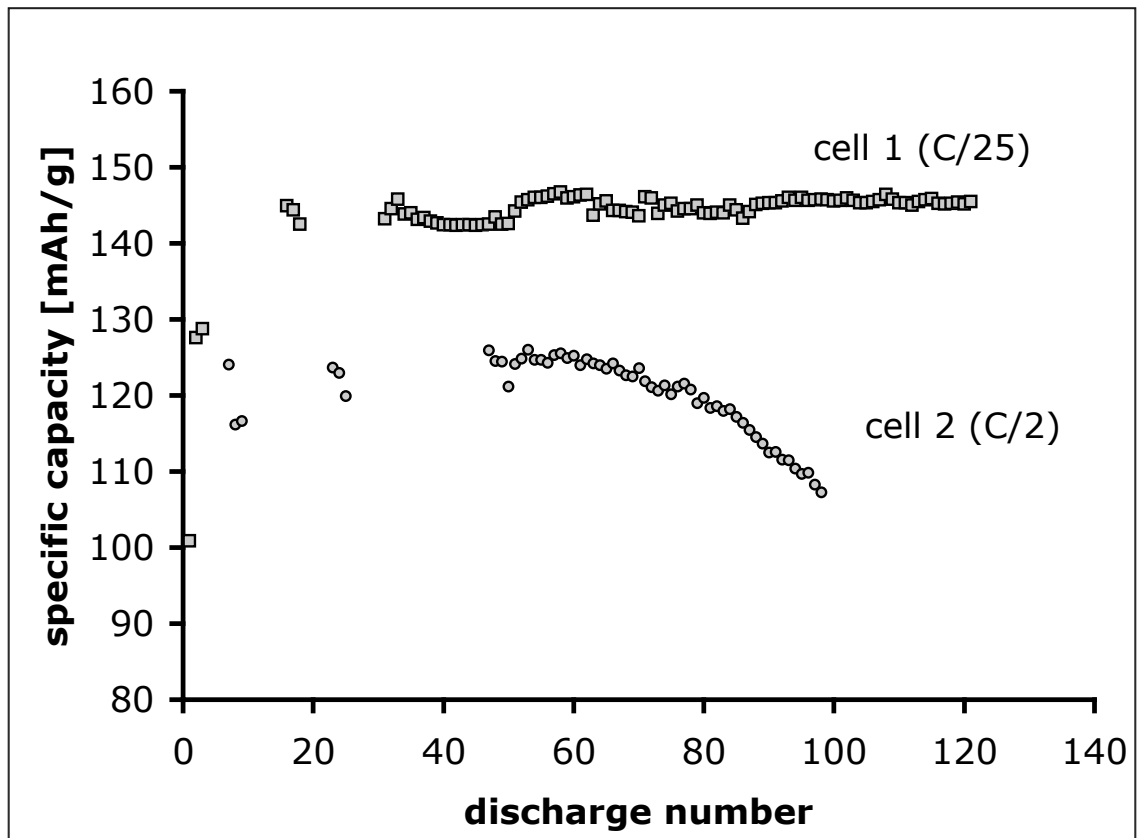
Figure 6, Arrangement of  $\text{PO}_4$  tetrahedra and  $\text{FeO}_6$  octahedra in  $\text{LiFePO}_4$  seen in the [001] projection. The representation illustrates the stacking of (100) and (001) planes.



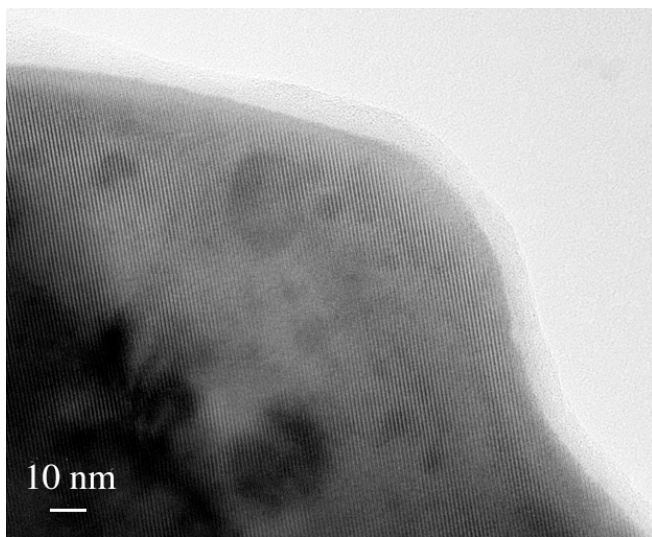
The bonds between the two sets of planes are marked by full circles for bonds between (010) planes and dashed circles for bonds between (100) planes.

Figure 7. Schematic drawing of an orthorhombic unit cell illustrating dislocation line direction and Burgers vector  $\vec{b}$  for  $\langle 100 \rangle$  type misfit dislocations in  $\{100\}$  type planes.

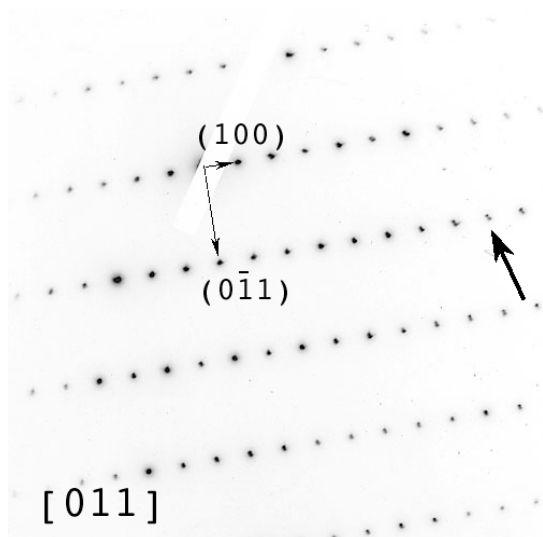
Figure 1



**Figure 2**

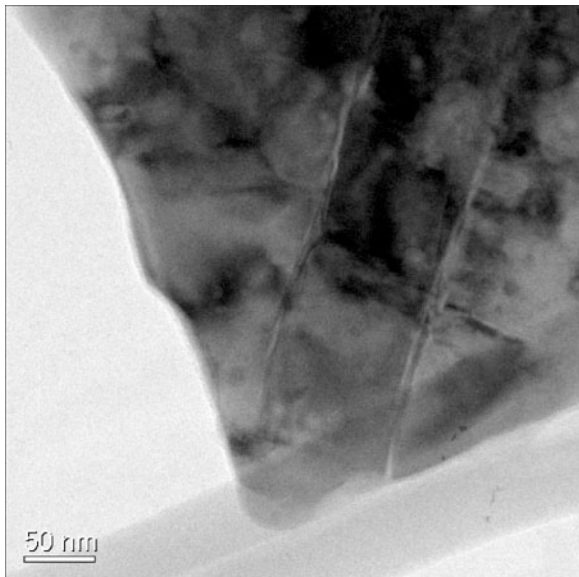


**a.)**

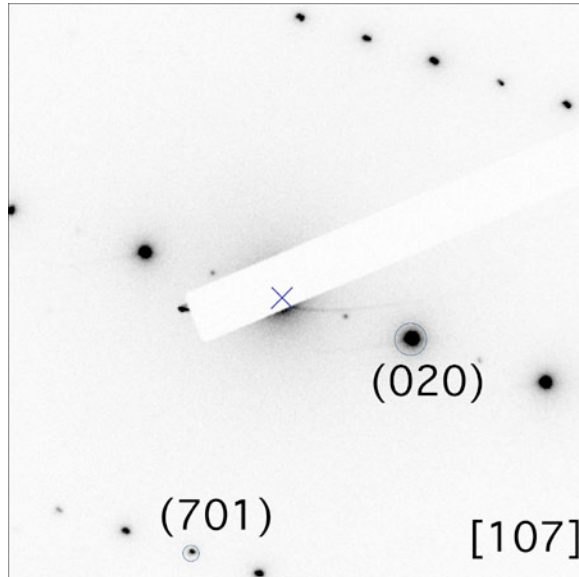


**b.)**

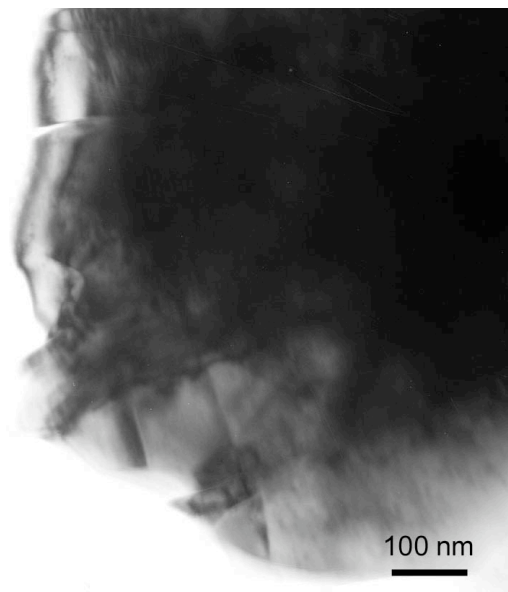
**Figure 3**



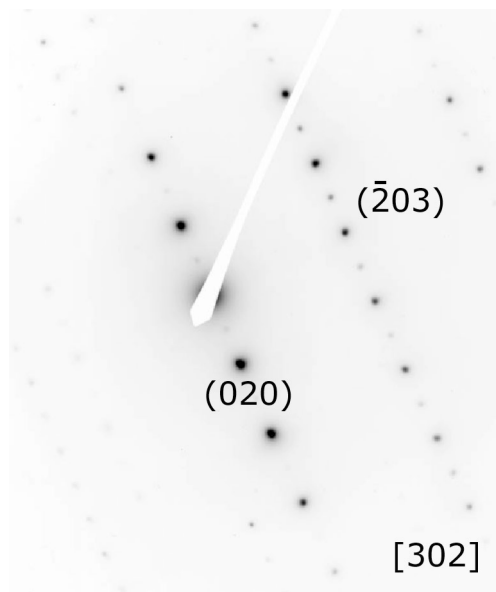
**a.)**



**b.)**

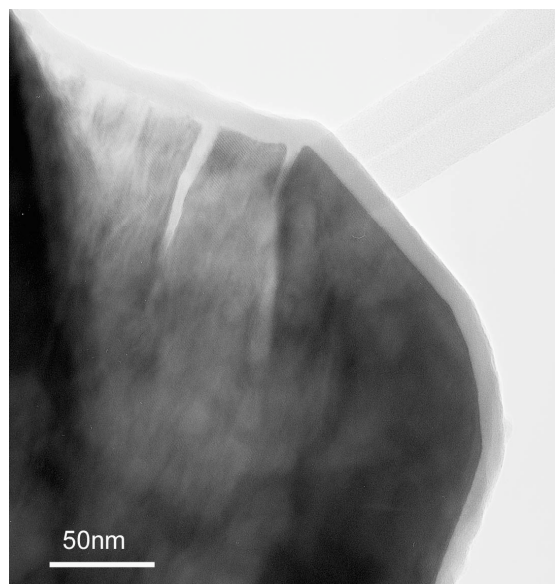


**c.)**

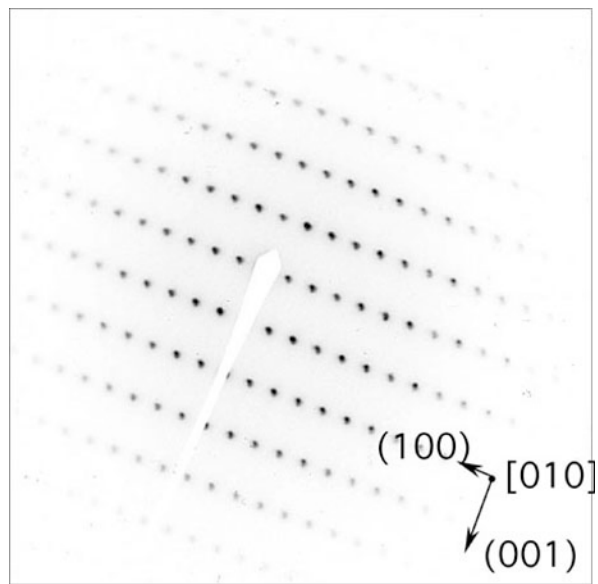


**d.)**

**Figure 4**

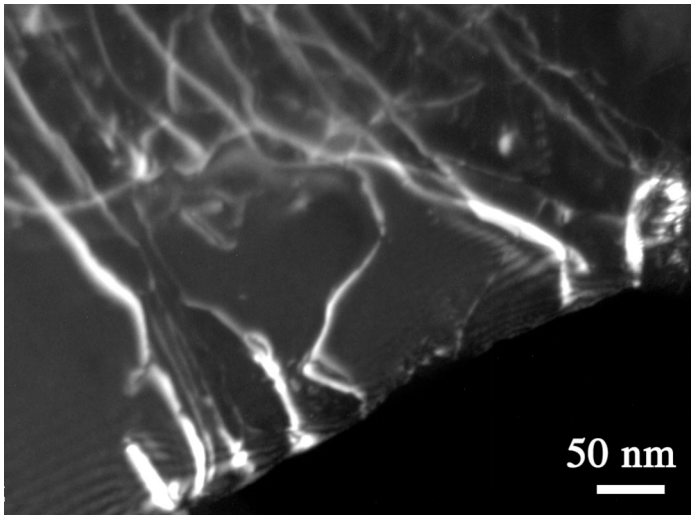


**a.)**

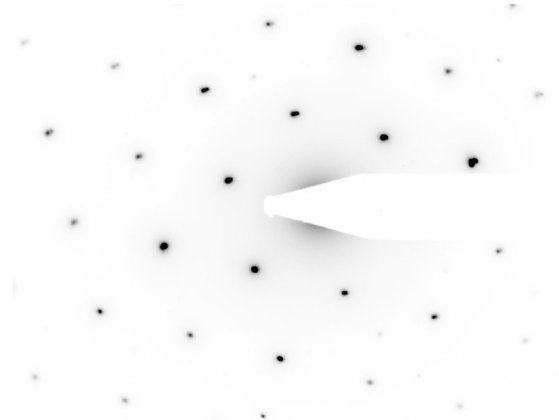


**b.)**

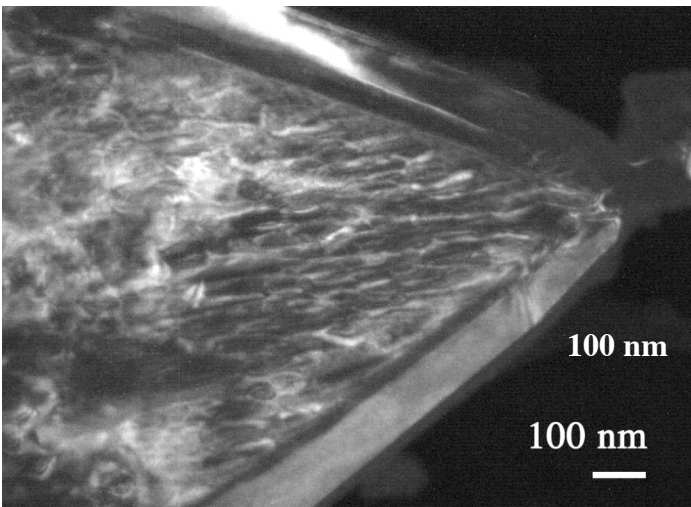
**Figure 5**



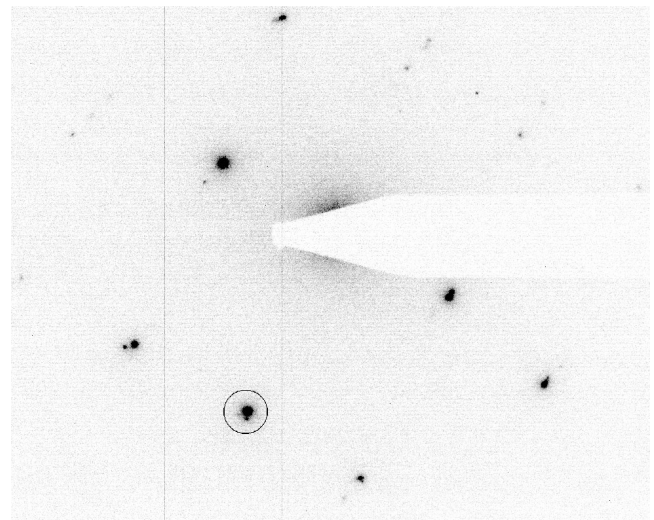
**a.)**



**b.)**



**c.)**



**d.)**

Figure 6

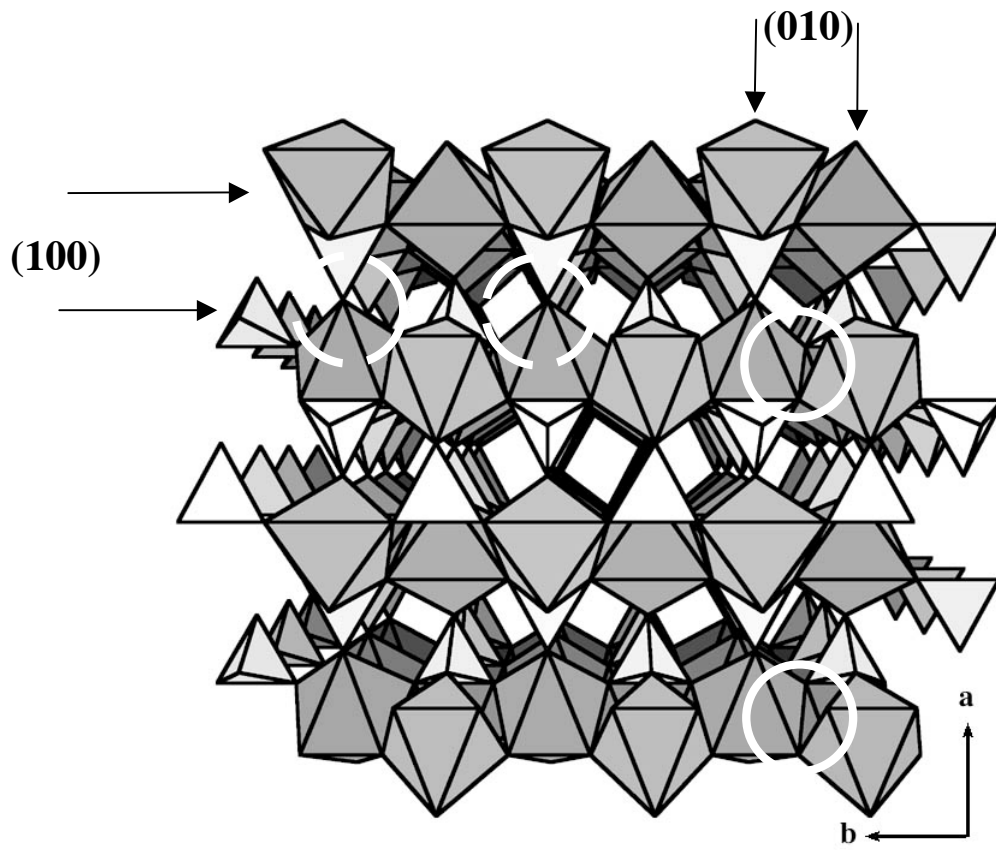


Figure 7

